One-dimensionally extended oxygen vacancy states in perovskite oxides

Naoki Tsunoda, Yu Kumagai, Masahiko Araki, and Fumiyasu Oba

One-dimensionally extended oxygen vacancy states in perovskite oxides

Naoki Tsunoda,[1] Yu Kumagai,[2, 3, *] Masahiko Araki,[1] and Fumiyasu Oba[1, 2, 4]

[1]*Laboratory for Materials and Structures, Institute of Innovative Research,*
Tokyo Institute of Technology, Yokohama 226-8503, Japan
[2]*Materials Research Center for Element Strategy, Tokyo Institute of Technology, Yokohama 226-8503, Japan*
[3]*PRESTO, Japan Science and Technology Agency, Tokyo 113-8656, Japan*
[4]*Center for Materials Research by Information Integration,*
Research and Services Division of Materials Data and Integrated System,
National Institute for Materials Science, Tsukuba 305-0047, Japan.
(Dated: February 14, 2019)

We elucidate as-yet-unidentified spatially extended oxygen vacancy states in ABO_3 perovskite oxides using first-principles calculations. When B sites are occupied with d^0 transition metal ions, charged oxygen vacancies are found to be long ranged in one direction because of charge transfer accompanied with atomic displacement along a chain-like structure. This finding offers two important results. First, it explains the reason why accurate calculations of oxygen vacancy formation energies necessitate very large supercells in d^0 perovskite and related oxides. It is remarkable especially for $KNbO_3$ and WO_3 on account of their anomalous Born effective charges. Second, such elongated vacancy states tend to show lower formation energies and thereby shallower donor levels. Our discussion is extendable to systems other than perovskites. Since the chain-like structure also appears in anatase TiO_2 but not in its rutile counterpart, it could be a reason why the oxygen vacancy is a double shallow donor in the former while constructing a deep state in the latter.

Perovskite oxides exhibit various fascinating physical properties, such as superconductivity [1], multiferroics [2], high dielectric constants, ferroelectricity, piezoelectricity [3], and ion conductivity [4]. They have also been commercially utilized for dielectric insulators in capacitors, piezoelectric actuators and sensors, ferroelectric random-access memory, and solid oxide fuel cells [3, 5]. Other future applications such as photocatalysts [6] and semiconductor devices [5, 7] are also proceeding. Oxygen vacancies (V_O) drastically affect the number of conducting electrons if they act as shallow donors and dominate the optical properties and carrier lifetimes if they form deep localized states inside the band gap. V_O should also determine the transport properties of ions such as O_2^- and H^+ and domain wall motion [8, 9]. Therefore, V_O are strongly connected not only to the physical properties but also to the material performances, e.g., insulation degradation, optical absorption, radiative recombination, phase stability, ion diffusivity, and domain switching. Uncovering the functional and detrimental behaviors of V_O and controlling their concentration is the key to understanding their rich physical properties in depth and achieving the best performances of the oxides. The main purpose of this Rapid Communications is to elucidate as-yet-unidentified one-dimensionally (1D) extended defect states of charged V_O in perovskite oxides based on first-principles calculations.

Figure 1(a–d) shows the doubly-ionized O vacancy (V_O^{2+})-induced atomic-site electrostatic potential that is the potential difference between the defective and defect-free bulk supercells ($V_{d/b}$). The $V_{d/b}$ values for rhombohedral $KNbO_3$ (KNO), tetragonal $SrTiO_3$ (STO) [10], cubic $BaSnO_3$ (BSO), and rhombohedral $LaAlO_3$ (LAO), which are ground-state structures, are shown (see Supplemental Material (SM) [11]

for other perovskite oxides). Generally, $V_{d/b}$ rapidly converges to the potential caused by the point-charge models (V_{PC}), although tiny constant shifts remain [12]. However, some atomic sites with large potential deviation reside in the defect region. In KNO and STO (Fig. 1(a, b)), one can see that $V_{d/b}$ obviously jumps at the O ions located on the B-O-B (B = Ti or Nb) 1D chain including V_O^{2+}. This indicates that the V_O^{2+} defect states elongate one-dimensionally in the chain direction, as illustrated in Fig. 1(e) (see SM [11] for additional details including the displacement distances). Based on our calculations, a similar tendency is found in other d^0 perovskite oxides such as $BaTiO_3$ (BTO) and WO_3, the latter of which takes the ReO_3 structure, namely the perovskite-related structure without A-site cations. Conversely, the elongation is not noticeable in BSO and is almost absent, except for the immediate neighbors of V_O^{2+}, in LAO. These results mean that the 1D-chain-like V_O^{2+} state does not arise in all the perovskite oxides.

Such upward shifts in the electrostatic potential are explained in terms of the Born effective charges (BECs). A BEC is defined as a derivative of polarization with respect to the relevant atomic displacement. BEC is determined from both a static ionic charge comprising a nucleus with tightly bound electrons and a dynamic charge transfer associated with the atomic displacement. The BECs of the O ions in the B ion direction ($Z^*_{O_\parallel}$) in the cubic phases are -10.1 in WO_3, -7.6 in KNO, -6.2 in BTO, and -5.5 in STO. These $Z^*_{O_\parallel}$ values are much smaller compared with the formal static charge of -2 and $Z^*_{O_\parallel}$ in BSO (-3.4), LAO (-2.4), and other typical oxides (In SM [11], BECs of selected oxides are tabulated). A smaller $Z^*_{O_\parallel}$ value means that more electrons are transferred from O to B ions when the B-O bond distance is decreased, and vice versa. B site cations also show large BEC values as counterparts of the O atoms ($Z^*_{B_\parallel}$ = 13.8, 10.0, 7.7, 6.7, 4.4, and 2.9 for WO_3, KNO, BTO, STO, BSO, and LAO, respec-
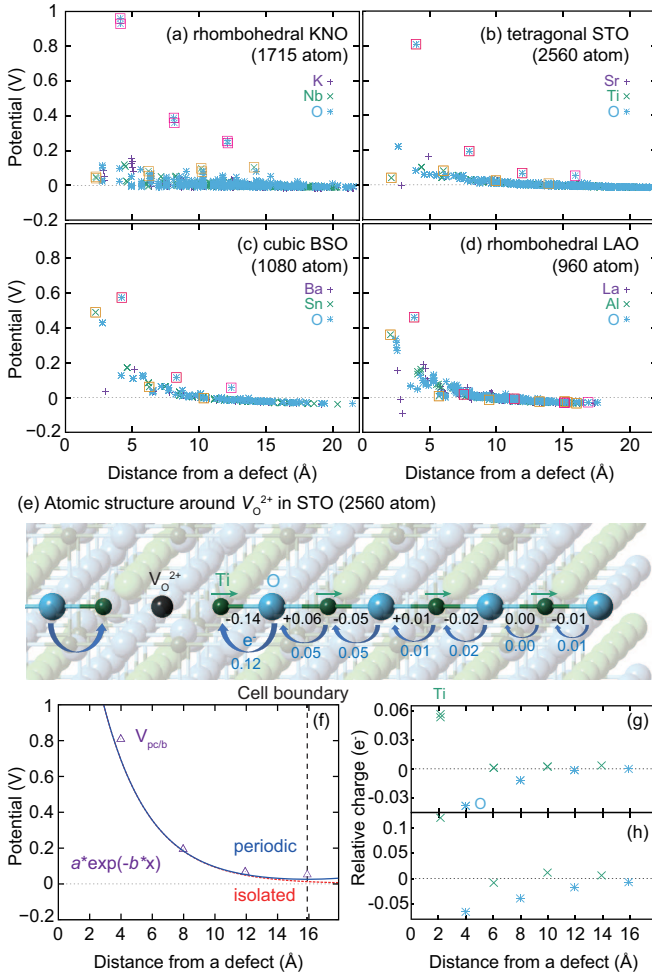
FIG. 1. Atomic-site electrostatic potential in supercells of (a) KNO, (b) STO, (c) BSO, and (d) LAO containing V_O^{2+} relative to that in the pristine bulk as a function of the distance from nearest V_O^{2+}. In (a–d), the values for the B-site and O atoms locating on the 1D-chain with V_O^{2+} are enclosed in yellow and red squares, respectively. (e) Atomic structure along the 1D extended V_O^{2+} state in STO. Changes of the bond lengths in Å and the charge transfer accompanied with the atomic displacement calculated using $Z_{O_\parallel}^*$ are also described with black and blue text, respectively (see text for details). Here, $Z_{O_\parallel}^* =$ -5.4 calculated in tetragonal STO is used for estimating n in Eq. (1). (f) Electrostatic potential at the atoms on the 1D extended V_O^{2+} state in the 2560-atom supercell of STO. Here, the point-charge model potential is subtracted. The fitted Slater-type function to the potential under consideration of the 1D periodic boundary condition and its isolated potential curve are also shown with solid blue and dashed red lines, respectively. (g) Change of the Bader charge in the STO 2560-atom supercell with V_O^{2+} from that in the bulk supercell; a positive value means an increase of the electron charge. (h) Net electron charge estimated from the change of the bond length, as in (e).

tively). The cause of the anomalous BECs is sensitivity of the hybridization between B-d and O-2p orbitals to the B-O distance [13]. Thus, the potential deviations at the O sites along one direction are a consequence of the electron transfer associated with the atomic displacement for screening the defect charge. It is also consistent with the results that $V_{d/b}$ in BSO

with moderate $Z_{O_\parallel}^*$ shows smaller but evident potential deviations (Fig. 1(c)) and is almost absent in LAO with $Z_{O_\parallel}^*$ much closer to the formal charge (Fig 1(d)).

Given the above discussion, one might expect $V_{d/b}$ at the B ions on the 1D-chain with V_O^{2+} to show a large deviation as well, but it is not seen in Fig. 1(a, b). This is because B ions largely displace outwardly along the B-O-B 1D chain, whereas O ions mostly remain at their original positions (see SM [11]). The reason why O ions mostly remain in place is probably because the neighboring B ions tend to push O ions outward, while positively charged V_O^{2+} attracts them inward. Consequently, the charge transfer from O to B ions is almost cancelled out except for the B ions next to V_O^{2+}, as illustrated in Fig. 1(e). This conclusion will also be confirmed with charge transfer analysis.

We next investigated the spatial distribution of the 1D chain-like defect. Figure 1(f) shows the relative electrostatic potential at the O ions on the 1D chain with V_O^{2+} in STO. Here, the potential caused by the periodic point charges and compensating background charge is subtracted to see the potential change caused by the charge transfer, referred to as $V_{d/PC}$. To determine the defect region, we fitted $V_{d/PC}$ with the Gaussian- and Slater-type functions, with expressions of $a\cdot\exp(-br^2)$ and $a\cdot\exp(-br)$, respectively (where a and b are fitting parameters). As shown in Fig. 1(f), we have found the Slater-type function fits well in the $V_{d/PC}$ (see SM [11] for the Gaussian-type function results) and presents the slowly decaying behavior of the V_O^{2+} in STO. The same behaviors are found in other d^0 perovskite oxides (see SM [11]).

A more straightforward approach to investigating the distribution is to analyze the change of the static atomic charge. We calculated the difference of the Bader charges [14, 15] in the defective and pristine supercells of STO (Fig. 1(g)). One can see the electron charge increases at the neighboring Ti sites, but remains nearly unchanged at the other Ti sites along the chain, which is consistent with the above discussion. Conversely, the electron charge decreases at the second-nearest O sites, and slowly decays with distance from V_O^{2+}.

To confirm that this charge redistribution is attributed to the charge transfer, we also calculated it from the change of the Ti-O distances and the dynamical charge of Z_O^*. In the case of 1D Ti-O chain-like structure, assuming the static ionic charge of O is -2 and the atomic displacement is small compared with the bond lengths, the transferred electron charge is:

$$n = \frac{1}{2}(Z_{O_\parallel}^* + 2) \cdot \frac{\Delta d_{Ti-O}}{d_{Ti-O}} \qquad (1)$$

where n is the transferred electron charge from an O ion to a Ti ion, d_{Ti-O} is the Ti-O bond length in the bulk, and Δd_{Ti-O} is the change of d_{Ti-O} caused by the atomic displacement. The net electron charge as a consequence of charge transfer quantified using Eq. (1) is shown in Fig. 1(h) (see the SM [11] for more details). As expected, the charge distribution is almost the same as that of the Bader charge analysis, although the absolute values are different by a factor of approximately two and the decay is slower.

Spatially extended V_O^{2+} offer two important consequences. Firstly, they lead to strong cell size dependences of V_O^{2+} for-
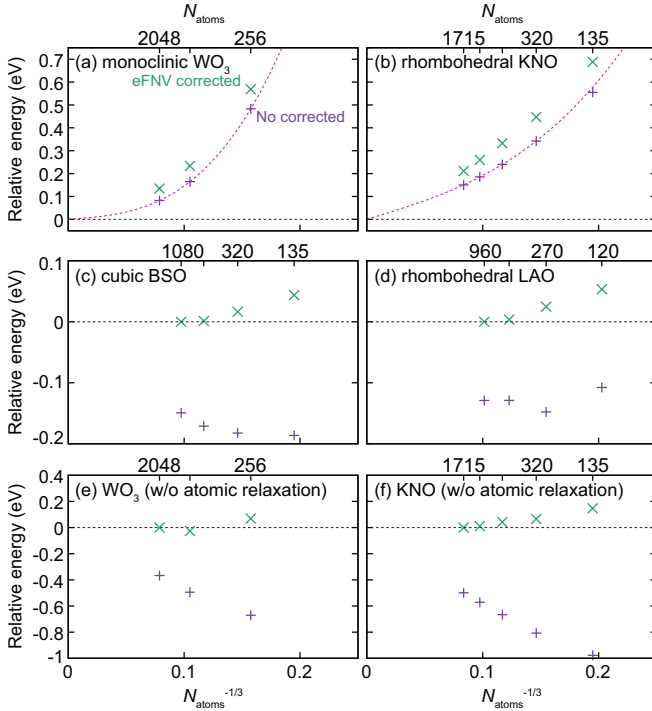
FIG. 2. (a–d) Relative V_O^{2+} formation energies ($E_f[V_O^{2+}]$) in (a) WO$_3$, (b) KNO, (c) BSO, and (d) LAO as a function of the supercell sizes. Two types of energies without (w/o) corrections and with eFNV corrections are shown. Note that scales in the y-axis are different. The numbers of atoms in the supercells are shown at the top of the figures. The supercells are constructed by isotropically expanding primitive unit cells, except for LAO (see SM [11] for details). (e, f) Same as in (a, b), but without atomic relaxation. The relative energy zero is set at the eFNV-corrected energy calculated using the largest supercell when the energy is converged, as in (c–f). Otherwise, it is set to the dilution limit estimated from the extrapolation, as in (a, b).

mation energies ($E_f[V_O^{2+}]$). Figure 2 shows $E_f[V_O^{2+}]$ that are calculated with various cell sizes in selected perovskite and related oxides. One can see the drastically decreasing tendency of $E_f[V_O^{2+}]$ with supercell size for WO$_3$ and KNO (Fig. 2(a, b)). In general, as the supercell size increases, $E_f[V_O^{2+}]$ tends to decrease and then increases starting at approximately 100 atoms [12, 16, 17]. Such a turning point is, however, absent at least up to a few thousand atoms in KNO and WO$_3$.

Recently, we have developed the extended Freysoldt–Neugebauer–Van de Walle finite supercell size-correction scheme for application to anisotropic systems, which is referred to as eFNV here [12, 18–21]. In principle, the eFNV scheme accurately corrects the finite size error caused by the spurious electrostatic interactions if the defect charge is fully contained in the supercell. However, elongated V_O states associated with anomalous BECs spatially overlap with their periodic images. Therefore, $E_f[V_O^{2+}]$ are not well corrected, even with a few thousand atom supercells in KNO and WO$_3$, which are in contrast with those in BSO and LAO (Fig. 2(c, d)). BTO and STO also show slightly slower convergence than typical oxides, consistent with their moderate spatial distribution of

V_O^{2+} (see SM [11]).

To corroborate our discussion, we have calculated the $E_f[V_O^{2+}]$ in WO$_3$ and KNO *without* atomic relaxations, as shown in Fig. 2(e, f). It should be noted that when the atomic positions are fixed, the energy dependence on the supercell size becomes larger because ionic screening of the electrostatic potential is absent (see uncorrected $E_f[V_O^{2+}]$ values in Fig. 2(e, f)). However, eFNV-corrected $E_f[V_O^{2+}]$ in WO$_3$ and KNO are calculated within errors of less than 0.07 and 0.15 eV with 256- and 135-atom supercells, respectively. These results strongly certify the scenario in which the 1D extended V_O^{2+} state is induced by the atomic displacement.

The second important consequence is that the extended state lowers the V_O^{2+} formation energy. From an electrostatics standpoint, defect formation energies decrease as the spatial distributions of the charged defects increase. Indeed, $E_f[V_O^{2+}]$ in WO$_3$, KNO, and STO aligned using the averaged core potential of the oxygen atoms are 3.45, 1.55, and 0.58 smaller than that in LAO, respectively, while those in BSO and LAO are the same within 0.1 eV. Extended V_O^{2+}, therefore, should be more stabilized compared with the neutral counterparts, meaning V_O tends to be a shallow donor. In fact, V_O shows a shallow behavior in WO$_3$, cubic BTO, and STO, whereas deep states are seen in BSO and LAO [22–27]. Of course, other factors such as dispersion of the conduction bands and orbital characteristics of the vacancy states influence the transition levels [28]. Therefore, V_O states are not necessarily shallow in all the perovskite oxides with anomalous BECs.

Extended V_O states are also expected to develop in other oxides that contain 1D chain-like structures and large BECs along the corresponding direction. One example is TiO$_2$. In rutile and anatase TiO$_2$ (r-TiO$_2$ and a-TiO$_2$), TiO$_6$ octahedra are shared at the corners and edges and Ti^{4+} takes d^0 electronic state. Anatase TiO$_2$ holds a pseudo-1D chain structure while r-TiO$_2$ does not (see Fig. 3(a, b)), and a-TiO$_2$ have smaller Z_O^* value of -5.1 along the chain direction (see SM [11] for the BEC tensors of TiO$_2$).

We calculated V_O^0, V_O^+, and V_O^{2+} in a- and r-TiO$_2$ using the Heyd-Scuseria-Ernzerhof (HSE06) hybrid functional. Firstly, we have confirmed that only a-TiO$_2$ shows the long-ranged large potential deviation along the chain (see the SM [11]), indicating V_O^{2+} exists as the extended state only in a-TiO$_2$. Figure 3 (c) shows the charge transition levels (CTL) of V_O. The energy levels were again aligned using the core potential of the oxygen atoms. Note that the 0.21 eV higher conduction band minimum (CBM) of the rutile in our calculation is comparable to 0.22 eV determined using X-ray photoelectron spectroscopy [33]. In r-TiO$_2$, the 2+/+ CTL exists within the band gap, while the 2+/+ CTL is 0.2 eV above the CBM in a-TiO$_2$ (see the Fig. 3 caption for the technical details). This means that the deep state in r-TiO$_2$ is not merely because of the relatively higher CBM in r-TiO$_2$. In addition, the $E_f[V_O^{2+}]$ is also lower in a-TiO$_2$ than in r-TiO$_2$, even though neutral V_O (V_O^0) shows 0.5 eV higher energy in a-TiO$_2$, as seen in Fig. 3(d). This decrease should be attributed to the reduction of $E_f[V_O^{2+}]$, caused by its 1D extended state, in a-TiO$_2$.
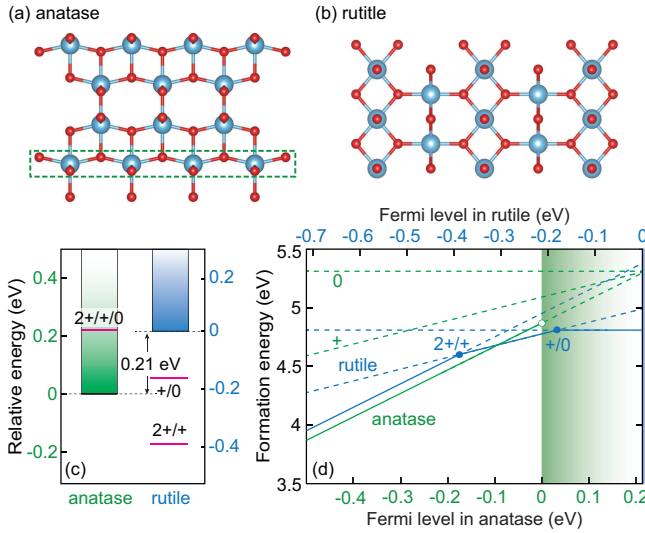
FIG. 3. Crystal structures of (a) anatase and (b) rutile TiO_2. A 1D chain-like structure is highlighted in (a). (c) Charge transition levels (CTLs) of V_O in anatase and rutile TiO_2. Note that +1 and neutral charge states in r-TiO_2 show the small polaronic nature, meaning one and two small polarons are trapped at the Ti sites, respectively, as reported in [29, 30]. The 2+/+/0 CTL in anatase TiO_2 is confirmed without sampling the conduction band minimum (CBM) using the Monkhorst-Pack k-point mesh (see Refs. [31, 32] for details). Note that the 2+/+ and +/0 CTLs in anatase are the same within the accuracy of the computations including corrections, so are connected as 2+/+/0 in (c). (d) $E_f[V_O^{2+}]$ as a function of the Fermi level near the CBM in anatase and rutile TiO_2. The open circle designates a shallow donor level corresponding to a hydrogenic state. The formation energies of the unstable charge states at a given Fermi level are shown with dashed lines. The zeros of the upper and lower x-axes are set to the aligned CBMs of rutile and anatase TiO_2, respectively. The calculations were performed using the HSE06 hybrid functional with 192- and 270-atom supercells for a- and r-TiO_2, respectively, as well as eFNV corrections (see SM [11] for the cell size dependencies of $E_f[V_O^{2+}$ in TiO_2). The oxygen chemical potential is set to the half of the energy of an O_2 molecule.

In conclusion, we have elucidated the 1D extended oxygen vacancy states in ABO_3 perovskite oxides. The origin is attributed to the dynamic charge transfers that occur between the B and O ions along the 1D-chain structure with V_O^{2+}. Our argument is backed up from atomic-site potential analyses and Bader charge and cell size dependencies of $E_f[V_O^{2+}]$ with and without atomic relaxation. We have also found that the elongated V_O state exponentially decays in real space and is not enclosed even in supercells containing a few thousand atoms for KNO and WO_3. Thus, we would like to warn of the need to revisit the V_O formation energies determined in previous studies. Furthermore, extended V_O^{2+} shows a relatively lower formation energy because of the large spatial charge distribution. Such energy lowering could contribute to shallow donor behaviors in WO_3, perovskite titanates, and a-TiO_2. Our findings hold generality in oxides with both d^0 transition metals and chain structures, and, therefore, give deeper insight into their point defects.

Methods. First-principles calculations were performed using the projector augmented wave (PAW) method [34], as implemented in VASP [35, 36]. The modified Perdew–Burke–Ernzerhof generalized gradient approximation tuned for solids [37] was used for calculating V_O^{2+} in the perovskite oxides. Hubbard U corrections [38] were adopted to the Ti-3d states in $SrTiO_3$ ($U_{\text{eff}} = 4.36$ eV [39, 40]). The HSE06 hybrid functional [41, 42] was also used for calculating the $E_f[V_O^q]$ (q=0, +, and 2+) values in a-TiO_2 and r-TiO_2. Spin polarization was considered for V_O^0 and V_O^+. Methods for calculating the defect formation energies and the details of the eFNV correction scheme can be found elsewhere [12, 31, 32]. To avoid other contributions to the electrostatic atomic site potentials and cell size dependences, only the ground state perovskite oxides were treated in this study; when a defect is introduced into a dynamically unstable phase, the defect formation energy and electrostatic potential may be drastically modified because of defect-induced symmetry lowering. The dynamical stability was checked using the first-principles phonon calculations with PHONOPY [43].

[1] H. W. R. Schooley, J. F. and M. L. Cohen, "Superconductivity in Semiconducting $SrTiO_3$," Phys. Rev. Lett. **12**, 474 (1964).

[2] S. V. Kiselev, R. P. Ozerov, and G. S. Zhdanov, "Detection of Magnetic Order in Ferroelectric $BiFeO_3$ by Neutron Diffraction," Soviet Physics Doklady **7**, 742 (1963).

[3] A. Bhalla, R. Guo, and R. Roy, "The perovskite structurea review of its role in ceramic science and technology," Materials Research Innovations **4**, 3 (2000).

[4] A. J. Jacobson, "Materials for solid oxide fuel cells," Chemistry of Materials **22**, 660 (2010).

[5] J. F. Scott, "Applications of modern ferroelectrics," Science **315**, 954 (2007).

[6] W. Wang, M. O. Tad, and Z. Shao, "Research progress of perovskite materials in photocatalysis- and photovoltaics-related energy conversion and environmental treatment," Chem. Soc. Rev. **44**, 5371 (2015).

[7] I. Grinberg, D. V. West, M. L. de Lázaro Torres, G. Gou, D. M. Stein, L. Wu, G. Chen, E. M. Gallo, A. R. Akbashev, P. K. Davies, J. E. Spanier, and A. M. Rappe, "Perovskite oxides for visible-light-absorbing ferroelectric and photovoltaic materials," Nature **503**, 509 (2013).

[8] K. Kreuer, "Aspects of the formation and mobility of protonic charge carriers and the stability of perovskite-type oxides," Solid State Ionics **125**, 285 (1999).

[9] A. Chandrasekaran, D. Damjanovic, N. Setter, and N. Marzari, "Defect ordering and defect–domain-

wall interactions in $PbTiO_3$: A first-principles study," Phys. Rev. B **88**, 214116 (2013).

[10] In the main text, we focus on only the $4a$ site in STO and one of the $4e$ sites in WO_3 denoted as O1 site in SM (see Supplemental Material for results for the other sites).

[11] See Supplemental Material at [URL will be inserted by publisher] for details of test sets, defect states, and derivation of Eq. (1).

[12] Y. Kumagai and F. Oba, "Electrostatics-based finite-size corrections for first-principles point defect calculations," Phys. Rev. B **89**, 195205 (2014).

[13] P. Ghosez, J.-P. Michenaud, and X. Gonze, "Dynamical atomic charges: The case of ABO_3 compounds," Phys. Rev. B **58**, 6224 (1998).

[14] R. Bader, *Atoms in Molecules: A Quantum Theory* (Oxford University Press, 1990).

[15] W. Tang, E. Sanville, and G. Henkelman, "A grid-based Bader analysis algorithm without lattice bias," J. Phys. Condens. Matter **21**, 084204 (2009).

[16] Third-order multipole contribution of the spurious electrostatic interactions, which usually increases the energy in a positively-charged vacancy model, is dominant when a supercell is small. However, the first-order term contribution, which decreases the energy, becomes dominant as the supercell size increases.

[17] The vacancy-induced elastic energy is relatively small; when both the lattice constants and atomic positions are fully relaxed, reduction of the formation energies are only 0.11 and 0.06 eV for 135-atom KNO and 256-atom WO_3 supercells, respectively.

[18] C. Freysoldt, J. Neugebauer, and C. G. Van de Walle, "Fully *Ab Initio* finite-size corrections for charged-defect supercell calculations," Phys. Rev. Lett. **102**, 016402 (2009).

[19] Y. Kumagai, M. Choi, Y. Nose, and F. Oba, "First-principles study of point defects in chalcopyrite $ZnSnP_2$," Phys. Rev. B **90**, 125202 (2014).

[20] Y. Kumagai, L. A. Burton, A. Walsh, and F. Oba, "Electronic structure and defect physics of tin sulfides: SnS, Sn_2S_3, and SnS_2," Phys. Rev. Applied **6**, 014009 (2016).

[21] N. Tsunoda, Y. Kumagai, A. Takahashi, and F. Oba, "Electrically benign defect behavior in zinc tin nitride revealed from first principles," Phys. Rev. Applied **10**, 011001 (2018).

[22] W. Wang, A. Janotti, and C. G. Van de Walle, "Role of oxygen vacancies in crystalline WO_3," J. Mater. Chem. C **4**, 6641 (2016).

[23] M. Choi, F. Oba, and I. Tanaka, "Electronic and structural properties of the oxygen vacancy in $BaTiO_3$," Appl. Phys. Lett. **98**, 172901 (2011).

[24] A. Janotti, J. B. Varley, M. Choi, and C. G. Van de Walle, "Vacancies and small polarons in $SrTiO_3$," Phys. Rev. B **90**, 085202 (2014).

[25] M. Choi, F. Oba, Y. Kumagai, and I. Tanaka, "Anti-ferrodistortive-Like Oxygen-Octahedron Rotation Induced by the Oxygen Vacancy in Cubic $SrTiO_3$," Adv. Mater. **25**, 86.

[26] D. O. Scanlon, "Defect engineering of $BaSnO_3$ for high-performance transparent conducting oxide applications," Phys. Rev. B **87**, 161201 (2013).

[27] M. Choi, A. Janotti, and C. G. Van de Walle, "Native point defects in $LaAlO_3$: A hybrid functional study," Phys. Rev. B **88**, 214117 (2013).

[28] W.-J. Yin, S.-H. Wei, M. M. Al-Jassim, and Y. Yan, "Prediction of the chemical trends of oxygen vacancy levels in binary metal oxides," Appl. Phys. Lett. **99**, 142109 (2011).

[29] P. Deák, B. Aradi, and T. Frauenheim, "Quantitative theory of the oxygen vacancy and carrier self-trapping in bulk TiO_2," Phys. Rev. B **86**, 195206 (2012).

[30] A. Malashevich, M. Jain, and S. G. Louie, "First-principles DFT + GW study of oxygen vacancies in rutile TiO_2," Phys. Rev. B **89**, 075205 (2014).

[31] Y. Kumagai, K. Harada, H. Akamatsu, K. Matsuzaki, and F. Oba, "Carrier-Induced Band-Gap Variation and Point Defects in Zn_3N_2 from First Principles," Phys. Rev. Applied **8**, 014015 (2017).

[32] Y. Kumagai, N. Tsunoda, and F. Oba, "Point defects and p-type doping in ScN from first principles," Phys. Rev. Applied **9**, 034019 (2018).

[33] D. Scanlon, C. Dunnill, J. Buckeridge, S. Shevlin, A. Logsdail, S. Woodley, C. Catlow, M. Powell, R. Palgrave, I. Parkin, G. Watson, T. Keal, P. Sherwood, A. Walsh, and A. Sokol, "Band alignment of rutile and anatase TiO_2," Nat. Mater. **12**, 798 (2013).

[34] P. E. Blöchl, "Projector augmented-wave method," Phys. Rev. B **50**, 17953 (1994).

[35] G. Kresse and J. Furthmüller, "Efficient iterative schemes for ab initio total-energy calculations using a plane-wave basis set," Phys. Rev. B **54**, 11169 (1996).

[36] G. Kresse and D. Joubert, "From ultrasoft pseudopotentials to the projector augmented-wave method," Phys. Rev. B **59**, 1758 (1999).

[37] J. P. Perdew, A. Ruzsinszky, G. I. Csonka, O. A. Vydrov, G. E. Scuseria, L. A. Constantin, X. Zhou, and K. Burke, "Restoring the density-gradient expansion for exchange in solids and surfaces," Phys. Rev. Lett. **100**, 136406 (2008).

[38] S. L. Dudarev, G. A. Botton, S. Y. Savrasov, C. J. Humphreys, and A. P. Sutton, "Electron-energy-loss spectra and the structural stability of nickel oxide: An LSDA+U study," Phys. Rev. B **57**, 1505 (1998).

[39] Z. Hou and K. Terakura, "Defect States Induced by Oxygen Vacancies in Cubic $SrTiO_3$: First-Principles Calculations," Journal of the Physical Society of Japan **79**, 114704 (2010).

[40] D. D. Cuong, B. Lee, K. M. Choi, H.-S. Ahn, S. Han, and J. Lee, "Oxygen Vacancy Clustering and Electron Localization in Oxygen-Deficient $SrTiO_3$: LDA+U Study," Phys. Rev. Lett. **98**, 115503 (2007).

[41] J. Heyd, G. E. Scuseria, and M. Ernzerhof, "Erratum: Hybrid functionals based on a screened coulomb potential," J. Chem. Phys. **124**, 219906 (2006).

[42] A. V. Krukau, O. A. Vydrov, A. F. Izmaylov, and G. E. Scuseria, "Influence of the exchange screening parameter on the performance of screened hybrid functionals," J. Chem. Phys. **125**, 224106 (2006).

[43] A. Togo and I. Tanaka, "First principles phonon calculations in materials science," Scr. Mater. **108**, 1 (2015).